

# 27%-Efficiency Four-Terminal Perovskite/Silicon Tandem Solar Cells by Sandwiched Gold Nanomesh

Ziyu Wang, Xuejie Zhu, Shengnan Zuo, Ming Chen, Cong Zhang, Chenyu Wang, Xiaodong Ren, Zhou Yang, Zhike Liu, Xixiang Xu, Qing Chang, Shaofei Yang, Fanying Meng, Zhengxin Liu, Ningyi Yuan, Jianning Ding, Shengzhong (Frank) Liu,\* and Dong Yang\*

Multijunction/tandem solar cells have naturally attracted great attention because they are not subject to the Shockley–Queisser limit. Perovskite solar cells are ideal candidates for the top cell in multijunction/tandem devices due to the high power conversion efficiency (PCE) and relatively low voltage loss. Herein, sandwiched gold nanomesh between MoO<sub>3</sub> layers is designed as a transparent electrode. The large surface tension of MoO<sub>3</sub> effectively improves wettability for gold, resulting in Frank–van der Merwe growth to produce an ultrathin gold nanomesh layer, which guarantees not only excellent conductivity but also great optical transparency, which is particularly important for a multijunction/tandem solar cell. The top MoO<sub>3</sub> layer reduces the reflection at the gold layer to further increase light transmission. As a result, the semitransparent perovskite cell shows an 18.3% efficiency, the highest reported for this type of device. When the semitransparent perovskite device is mechanically stacked with a heterojunction silicon solar cell of 23.3% PCE, it yields a combined efficiency of 27.0%, higher than those of both the sub-cells. This breakthrough in elevating the efficiency of semitransparent and multijunction/tandem devices can help to break the Shockley–Queisser limit.

## 1. Introduction

The crystalline Si-based solar cells have been dominating the ever-expanding global photovoltaic (PV) market with about 95% market share. With its highest cell efficiency of 26.6% reaching its theoretical limit, there is little hope to further raise its performance by just device optimization within the single-junction cell architecture. As the PV market is so huge with its annual revenue in the order of trillion US dollars, even 1% cost reduction would mean net profit of billions of US dollars per year. Since efficiency increase is proven to be the most reliable means to reduce cost, it makes sense for industries to develop tandem cells with potential of significantly increased cell efficiency.

Within the last few years, organic–inorganic lead halide perovskite solar cells

Z. Wang, Prof. S. Liu  
Dalian National Laboratory for Clean Energy  
iChEM  
Dalian Institute of Chemical Physics  
Chinese Academy of Sciences  
457 Zhongshan Road, Dalian 116023, China  
E-mail: szliu@dicp.ac.cn

Z. Wang  
University of Chinese Academy of Sciences  
Beijing 100049, China

X. Zhu, S. Zuo, Dr. M. Chen, C. Zhang, C. Wang, Dr. X. Ren, Dr. Z. Yang,  
Prof. Z. Liu, Prof. S. Liu, Prof. D. Yang  
Key Laboratory of Applied Surface and Colloid Chemistry  
Ministry of Education  
Shaanxi Engineering Lab for Advanced Energy Technology  
School of Materials Science and Engineering  
Shaanxi Normal University  
Xi'an 710119, China  
E-mail: szliu@dicp.ac.cn; dongyang@snnu.edu.cn

Dr. X. Xu, S. Yang  
Hanergy Thin Film Power Group Ltd.  
Chengdu R&D Center  
Chengdu, Sichuan 610200, China

Q. Chang  
Hanergy Mobile Energy Holding Group  
Beijing 100107, China

Prof. F. Meng, Prof. Z. Liu  
Research Center for New Energy Technology  
Shanghai Institute of Microsystem and Information Technology (SIMIT)  
Shanghai 200050, China

Prof. N. Yuan, Prof. J. Ding  
School of Materials Science and Engineering  
Jiangsu Collaborative Innovation Center of Photovoltaic Science  
and Engineering  
Jiangsu Province Cultivation Base for State Key Laboratory  
of Photovoltaic Science and Technology  
Changzhou University  
Changzhou 213164, China

 The ORCID identification number(s) for the author(s) of this article can be found under <https://doi.org/10.1002/adfm.201908298>.

DOI: 10.1002/adfm.201908298

(Pvs-SCs) have outpaced all other PVs in terms of power conversion efficiency (PCE), with the laboratory record standing at 25.2%.<sup>[1–11]</sup> Although the record efficiency of Pvs-SCs has been increasing with unprecedented incremental speed, the highest PCE remains limited by the Shockley–Queisser limit of about 33% for a single junction cell.<sup>[12]</sup> In order to further enhance the PCE of solar cells, multijunction/tandem PV devices have been developed.<sup>[13–15]</sup> A multijunction/tandem solar cell is comprised of a top cell with a large-bandgap absorber to effectively convert short wavelength spectrum with minimized thermalization loss and a bottom cell with the narrow-bandgap absorber to harvest near-infrared photons to maximize current density. When the device is illuminated by sunlight, the top cell absorbs the short wavelength photons with energies higher than its bandgap to generate a high open-circuit voltage ( $V_{oc}$ ), and the low-bandgap bottom cell absorbs the long wavelength photons with energies between the bandgaps of the top cell and bottom cell. This could reduce thermalization loss as well as photon loss, and provide an efficiency limit of 46% under the standard solar spectrum and intensity.<sup>[16]</sup>

To date, the market-proven heterojunction silicon solar cell is a promising bottom cell since it provides excellent spectral responsivity in the near-infrared region. A perovskite device holds the most potential as a top cell for a double junction solar cell owing to its merits of high absorption coefficient ( $\approx 10^5 \text{ cm}^{-1}$ ), high carrier mobility, low trap density (approximately  $10^{14} \text{ cm}^{-3}$  for microcrystalline thin film and  $10^{10} \text{ cm}^{-3}$  for single-crystal), tunable bandgap (from 1.17 to 2.24 eV), low cost, easy fabrication, etc.<sup>[17–25]</sup> There are three main configurations for multijunction/tandem solar cells: spectral splitting, monolithically integrated, and mechanically stacked devices.<sup>[26]</sup> The spectral splitting cell exhibits the highest potential PCE exceeded 28% since it has the minimal parasitic absorption loss due to the reduction of recombination layers and a transparent back electrode in an optically splitting system.<sup>[27]</sup> However, an optical splitting system is at present too expensive, leading to unlikely short-term commercialization. The two-terminal (2T) monolithically integrated cell with a perovskite top cell and a silicon bottom cell has developed rapidly to decrease the cost of production. Sahli et al. adopted a two-step process of co-evaporating and spin-coating to produce the perovskite on the c-Si pyramids, and the efficiency of 2T tandem device was up to 25.2%.<sup>[28]</sup> Snaith worked in Oxford PV has reported a record efficiency of 2T tandem cell is also up to 28%.<sup>[29]</sup> Even though 2T cells have achieved great success, major challenges remain in the deposition of the high-quality perovskite absorbers and recombination layers onto the inverted-pyramidal-nanostructure surface of the present silicon devices.

A mechanically stacked four terminal (4T) multijunction/tandem solar cell solves these issues successfully because the perovskite top cell and silicon bottom cell are optically coupled and electrically independent, so each sub-cell can work at its maximum power point with no need for current matching, implying that the recombination layer is not necessary. Also, the perovskite absorber could be directly deposited on the smooth substrate in 4T multijunction/tandem solar cell.

From the above analysis, a feasible transparent electrode technology becomes an urgent problem for 4T multijunction/tandem solar cells for practical application. The commonly used

transparent metal oxide electrodes such as indium tin oxide (ITO), indium zinc oxide, and Al-doped zinc oxide are typically fabricated by magnetron sputtering, but this technique is harmful to the underlying organic interface layers and perovskite absorbers, and thus, buffer layers are needed to prevent degradation in the performance of the corresponding Pvs-SCs. Ultrathin metal films (<10 nm thick) deposited by thermal evaporation could replace the transparent metal oxide electrodes and would not require buffer layers because of the more moderate process.<sup>[30–34]</sup> However, this type of electrode exhibits inferior conductivity due to the discontinuous layer and strong reflection because of very smooth surface. Up to date, the record PCEs for semitransparent devices and 4T multijunction/tandem cells utilizing an ultrathin metal film reached to 18.1% and 27.1% by optimizing the transparent electrodes and passivating the interface.<sup>[35,36]</sup>

In this work, the molybdenum trioxide ( $\text{MoO}_3$ ) sandwiched gold nanomesh to form  $\text{MoO}_3/\text{Au}/\text{MoO}_3$  multilayer fabricated by mild thermal evaporation, which could not destroy underneath layer, is developed as an electrode for semitransparent Pvs-SC. The ultrathin gold nanomesh layer on the  $\text{MoO}_3$  achieves the optimized transparency and conductivity. Meanwhile, the top  $\text{MoO}_3$  layer acts as an antireflection layer for minimized light loss. As a result, the efficiency of the semitransparent Pvs-SCs is increased to 18.3%, the highest value for this type of devices. When the semitransparent perovskite device is mechanically stacked with a heterojunction silicon solar cell, it yields a combined efficiency of 27.0% for the multijunction/tandem cell, one of the highest reported for this type of multijunction/tandem cells.

## 2. Results and Discussion

### 2.1. Growth Mechanism and Properties of the Transparent Top Electrode

In general, organic materials<sup>[37]</sup> such as 2,2',7,7'-tetrakis(*N,N*-di-*p*-methoxyphenylamine)-9,9'-spirobifluorene (spiro-OMeTAD) exhibit the small surface tension, which leads to the weak interaction between gold atoms and spiro-OMeTAD substrate. The gold atoms will accumulate onto the spiro-OMeTAD substrate to form the gold islands according to Volmer–Weber growth principle,<sup>[33]</sup> as shown in Figure 1a. Molybdenum oxide has been introduced to improve the gold wettability because of the large surface tension ( $\approx 200 \text{ mN m}^{-1}$ ),<sup>[38]</sup> which results in Frank–van der Merwe growth (Figure 1b) to form an ultrathin gold film on the molybdenum oxide. We used thermal evaporation to deposit molybdenum oxide, and its stoichiometry was performed on X-ray photoelectron spectroscopy, as shown in Figure S1 in the Supporting Information. The ratio of Mo and O was calculated as 0.33, the chemical formula of layer is thereby described as  $\text{MoO}_3$  with negligible error. The details can be seen in the Supporting Information. The transmission of  $\text{MoO}_3$  with different thickness has already shown in Figure S2a in the Supporting Information. It is apparent that the transmission decreases with increasing the thickness of  $\text{MoO}_3$ . However, when the thickness of  $\text{MoO}_3$  is less than 30 nm, it cannot completely cover the substrate (Figure S2b,c, Supporting Information). Figure S3 in the Supporting Information shows the

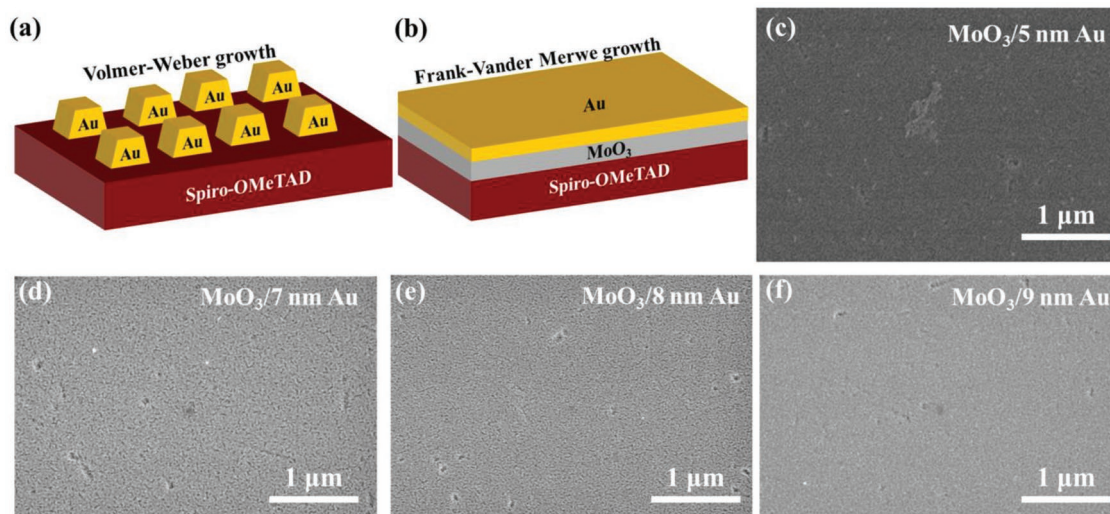


**Figure 1.** A cartoon showing how the gold grows on a) spiro-OMeTAD and b) MoO<sub>3</sub> substrates. SEM images of gold deposited on MoO<sub>3</sub> substrates with the thickness of c) 5 nm, d) 7 nm, e) 8 nm, and f) 9 nm.

energy-dispersive X-ray mappings of different thickness of MoO<sub>3</sub> deposited on spiro-OMeTAD. It is apparent that Mo elements widely disperse on spiro-OMeTAD substrate when the thickness of MoO<sub>3</sub> is 20 nm. However, Mo elements almost completely cover the spiro-OMeTAD substrate when the thickness is up to 30 nm, in good agreement with the scanning electron microscope (SEM) measurements (Figure S2, Supporting Information). Thus, we fixed the thickness of MoO<sub>3</sub> at 30 nm because at this thickness it has good transparency and full surface coverage. The atomic force microscope (AFM) was used to detect the morphology of gold layers deposited on spiro-OMeTAD and MoO<sub>3</sub> surface. Figure S4 in the Supporting Information shows the AFM images of gold layers on different substrates. When the gold grows on spiro-OMeTAD, it forms separated small islands with some holes. While the gold deposits on MoO<sub>3</sub> surface, it generates the linked nanomesh layer due to producing the large gold grain size. The results further demonstrate above analysis. Figure 1c–f shows the SEM images of different thicknesses of gold deposited on MoO<sub>3</sub> substrates. The gold forms discrete nanoparticles and cannot cover the MoO<sub>3</sub> substrate when its thickness is less than 7 nm; whereas for thicknesses greater than 7 nm, it forms a nanomesh layer, and the pore diameter of the nanomesh decreases with increasing thickness. The linked gold nanomesh structure will improve the conductivity and transparency, both of which are critical for achieving high-efficiency semitransparent Pvs-SCs.

**Figure 2a** shows the conductivity of different thicknesses of gold coated on MoO<sub>3</sub>, and the parameters are summarized in Table S1 in the Supporting Information. When the thickness of gold is 5 nm, the largest sheet resistance of 47.5 Ω sq<sup>-1</sup> is produced due to independent gold nanoparticles. The sheet resistance decreases to 10.0 Ω sq<sup>-1</sup> when the thickness of gold increases to 9 nm. The good conductivity originates from the formation of a linked gold nanomesh structure, in good agreement with the SEM results.

The transmittance spectra of different thicknesses of gold deposited on MoO<sub>3</sub> substrates are measured by UV-vis spec-

troscopy, as shown in Figure 2b. As expected, the transmission decreases with increasing gold thickness. In the present study, a 7 nm thick gold nanomesh layer deposited on MoO<sub>3</sub> substrate is employed to make the best tradeoff between the transparency and conductivity. Although this MoO<sub>3</sub>/Au multilayer has a small sheet resistance (19.6 Ω sq<sup>-1</sup>, comparable with commercial ITO), its average transmission is only about 56% in the wavelength range from 800 to 1100 nm. The low transmission in the near-infrared region would block photons from reaching the silicon bottom cell, hindering the improvement of efficiency for multijunction/tandem solar cells. Therefore, the transparency of MoO<sub>3</sub>/Au needs to be further enhanced. An additional MoO<sub>3</sub> layer caps the MoO<sub>3</sub>/Au as an antireflection layer because its refractive index of ≈2.03 is between those of the gold nanoparticles at ≈2.35 and air.<sup>[39,40]</sup> Figure 2c shows the transmission spectra of MoO<sub>3</sub>/Au/MoO<sub>3</sub> for various thicknesses of the top MoO<sub>3</sub> layer. The figure shows that the average transmission reaches approximately 74% in the wavelength range of 800–1100 nm when the thickness of top MoO<sub>3</sub> is 80 nm. The reflection spectra for different thickness of top MoO<sub>3</sub> is also shown in Figure 2c. It is clear that the lowest reflection from 800 to 1200 nm was obtained when the thickness of top MoO<sub>3</sub> reached to 80 nm. The theoretical simulation results further confirm the good transmission based on 80 nm thick top MoO<sub>3</sub>, as shown in Figure S5 in the Supporting Information. The detailed simulation is described in the Supporting Information. The good transparency in the near-infrared region is beneficial to improving the photocurrent of silicon bottom devices in multijunction/tandem solar cells.

## 2.2. Device Design and Characterization of Semitransparent Pvs-SCs

The suitable transparency and good conductivity of the multilayer electrodes inspire us to fabricate semitransparent Pvs-SCs. The semitransparent device structure is shown in

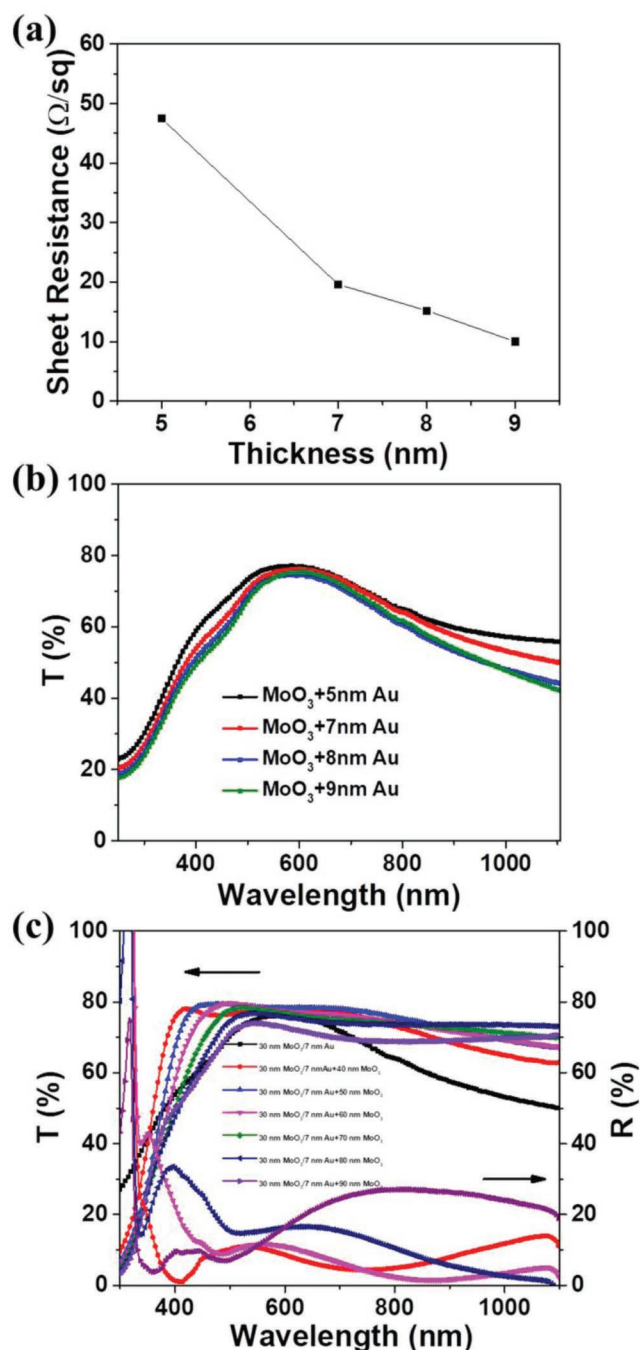


**Figure 2.** a) Sheet resistance and b) transmittance spectra for the different thicknesses of gold layers deposited on MoO<sub>3</sub> substrates. c) Transmittance and reflection spectra for the different thicknesses of MoO<sub>3</sub> films coated on the gold surface.

Figure S6a in the Supporting Information, where ITO is used as the cathode, TiO<sub>2</sub> is employed as the electron transport layer, methylammonium lead triiodide (MAPbI<sub>3</sub>) acts as the absorber (the morphology of MAPbI<sub>3</sub> is shown in Figure S7a in the Supporting Information, and its X-ray diffraction pattern is given in Figure S7b in the Supporting Information), spiro-OMeTAD serves as the hole transport layer, MoO<sub>3</sub>/

ultrathin Au is used as the top contact, and the top MoO<sub>3</sub> is introduced as an antireflection layer. An opaque perovskite device is also fabricated for comparison to the semitransparent cell, and its structure is shown in Figure S6b in the Supporting Information. Figure 3a gives the current density–voltage ( $J$ – $V$ ) characteristics of the semitransparent and opaque Pvs-SCs, and the parameters are summarized in Table 1. The opaque perovskite device shows a short-circuit current density ( $J_{sc}$ ) of 22.3 mA cm<sup>-2</sup>, a  $V_{oc}$  of 1137 mV, and a fill factor of 82.2%, yielding a PCE of 20.8%. The incident-photon-to-charge-conversion efficiency (IPCE) of opaque device is shown in Figure S8 in the Supporting Information, and the calculated photocurrent is 22.1 mA cm<sup>-2</sup>, very close to the  $J$ – $V$  curves. The PCE of the semitransparent perovskite cell is up to 18.3% under the reverse scan direction with a  $J_{sc}$  of 19.8 mA cm<sup>-2</sup>,  $V_{oc}$  of 1156 mV, and FF of 79.9%, which is the highest efficiency for semitransparent Pvs-SCs to date. While using the forward scan direction, the efficiency reduces to 17.0% with  $J_{sc}$  = 19.7 mA cm<sup>-2</sup>,  $V_{oc}$  = 1114 mV, and FF = 77.4% (Figure S9, Supporting Information), decreased by about 7%. We believe the hysteresis originates from the ion migration and trap-state density within the perovskite absorber.<sup>[2,11]</sup> The efficiency is confirmed by tracking the measured stable photocurrent for opaque and semitransparent perovskite devices biased at the maximum power point voltages of 1001 and 982 mV, respectively, as shown in Figure 3b. The stabilized PCEs of the opaque and semitransparent devices are 20.8% and 18.1%, in excellent accordance with  $J$ – $V$  measurements. The stability of the semitransparent perovskite device is also studied, as shown in Figure S10 and Table S2 in the Supporting Information. When the device stored in the air under dark for 172 h, the efficiency keeps about 95% of its initial value, indicating the good long-term stability.

The lower efficiency of the semitransparent device compared to the opaque one is mainly caused by decreased  $J_{sc}$  and a lesser extent reduced FF. The smaller FF of the semitransparent Pvs-SC, seen as a less sharp decrease in current with increasing forward bias in Figure 3a, can be attributed to the lower conductivity of the ultrathin gold nanomesh layer compared with that of the thick gold film in the opaque device. The decreased  $J_{sc}$  comes from the relatively high transmission of the semitransparent device compared with that of the opaque device (Figure S11, Supporting Information). In an opaque cell with a thick gold layer (80 nm) as the back electrode, the thick gold layer plays the role of back reflector. When the light passes through the perovskite absorber, the unabsorbed photons arrive at the back electrode and can be reflected back to the absorber, thus increasing the path length of photons traversing the absorber. However, a portion of the light passes through the back electrode in the semitransparent device, leading to some photon loss. Interestingly, the  $V_{oc}$  of the semitransparent Pvs-SC increases to 1156 mV from 1137 mV of the opaque perovskite device. Figure 3c,d shows the energy level alignments of both the opaque and semitransparent devices. It is clear that the offset between the electron and hole transport layers significantly increases when MoO<sub>3</sub> is introduced. This large offset provides extra energy for carrier transfer to reduce both charge recombination and energy loss, leading to higher  $V_{oc}$  in the semitransparent device.<sup>[41–43]</sup>

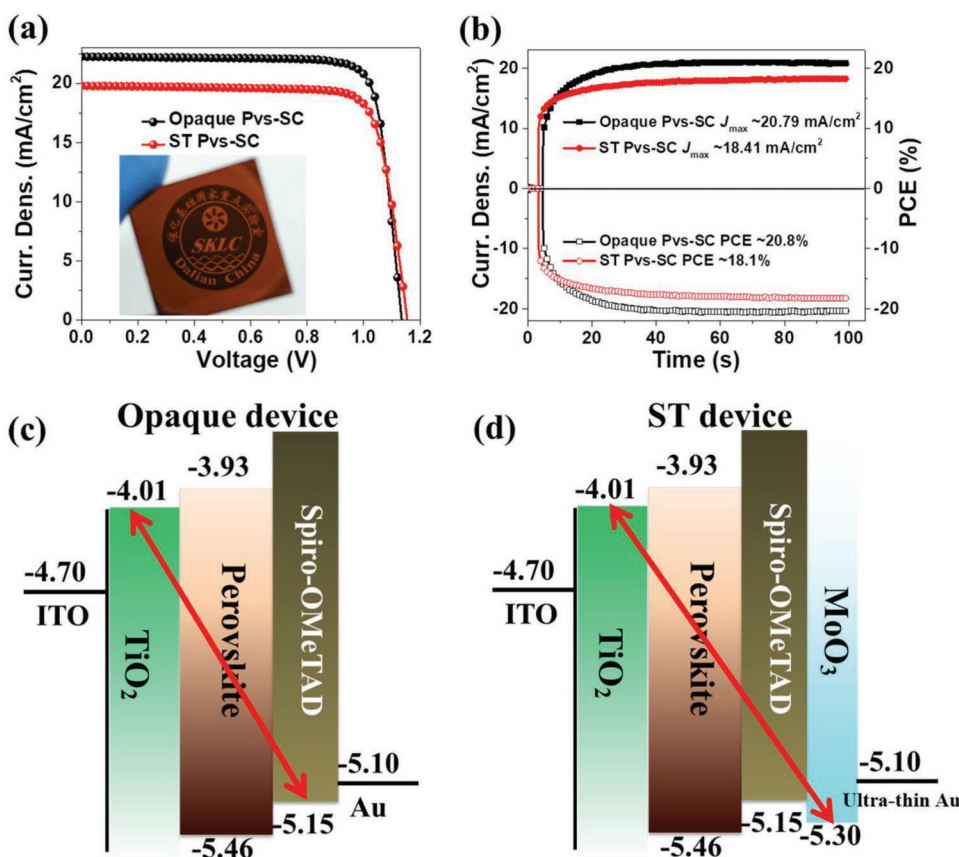


**Figure 3.** a)  $J$ - $V$  characteristics of semitransparent and opaque Pvs-SCs; the inset is a picture of a semitransparent device. b) Photocurrents and PCEs versus time for semitransparent and opaque perovskite devices biased at the maximum power point voltages of 982 and 1001 mV, respectively. Energy level alignments of c) opaque and d) semitransparent perovskite devices. The values of conduction band and valence band for different materials are from refs. [22,24,25,42].

### 2.3. Four-Terminal Perovskite/Silicon Tandem Solar Cells

Combining the highest-efficiency semitransparent perovskite devices and commercial silicon heterojunction solar cells, mechanically stacked 4T multijunction/tandem solar cells were fabricated. Figure 4a shows the configuration of the 4T multijunction/tandem solar cell. The sunlight is incident from the ITO/TiO<sub>2</sub> side of the perovskite top cell, and photons with short wavelength are captured by perovskite cell, while the long

**Table 1.** Summary of PV parameters for different types of solar cells and the summed 4T perovskite/silicon multijunction/tandem device (the active areas of opaque and semitransparent perovskite devices is 0.096 cm<sup>2</sup>, the area of silicon cell is 1.00 cm<sup>2</sup> cutting by laser, and the 1 cm<sup>2</sup> perovskite device is just used to mask the silicon cell).

Solar cell	$V_{oc}$ [mV]	$J_{sc}$ [mA cm <sup>-2</sup> ]	FF [%]	PCE [%]
Opaque Pvs-SC	1137	22.3	82.2	20.8
Semitransparent perovskite top cell	1156	19.8	79.9	18.3
Si heterojunction solar cell	708	41.1	80.3	23.3
Filtered silicon bottom cell	698	15.6	80.1	8.7
Multijunction/tandem solar cell	-	-	-	27.0

wavelength photons pass through the top cell into the silicon bottom cell to be converted into electrical energy. Figure 4b shows the  $J$ - $V$  curves of the perovskite top cell, silicon cell, and filtered silicon cell (by the top cell), and the parameters are summarized in Table 1. The stand-alone heterojunction silicon solar cell has a PCE of 23.3%. The efficiency of the silicon bottom cell decreases to 8.7% after being filtered by the perovskite top cell. The transmission spectrum of the perovskite top cell is shown in Figure S12 in the Supporting Information. It is apparent that most (but not all) of the short-wavelength light (energy above the perovskite bandgap) has been absorbed by the perovskite top cell and a substantial portion of the long-wavelength light is blocked by the top cell, both of which leads to the reduced  $J_{sc}$  (from 41.1 to 15.6 mA cm<sup>-2</sup>) of the silicon bottom cell. Figure 4c shows the IPCE of the semitransparent perovskite top cell and filtered silicon bottom cell. The integrated photocurrents are 19.3 and 14.9 mA cm<sup>-2</sup> for the perovskite top cell and silicon bottom cell, respectively, very close to the  $J$ - $V$  measurements. Since the intensity of illumination reaching the silicon bottom cell is lower than for the stand alone silicon device, the photon-induced charge carrier concentration is reduced, resulting in a slightly decreased  $V_{oc}$ .<sup>[44-46]</sup> As a result, the summed PCE of the 4T perovskite/silicon multijunction/tandem cell is up to 27.0%, higher than both independent sub-cells.

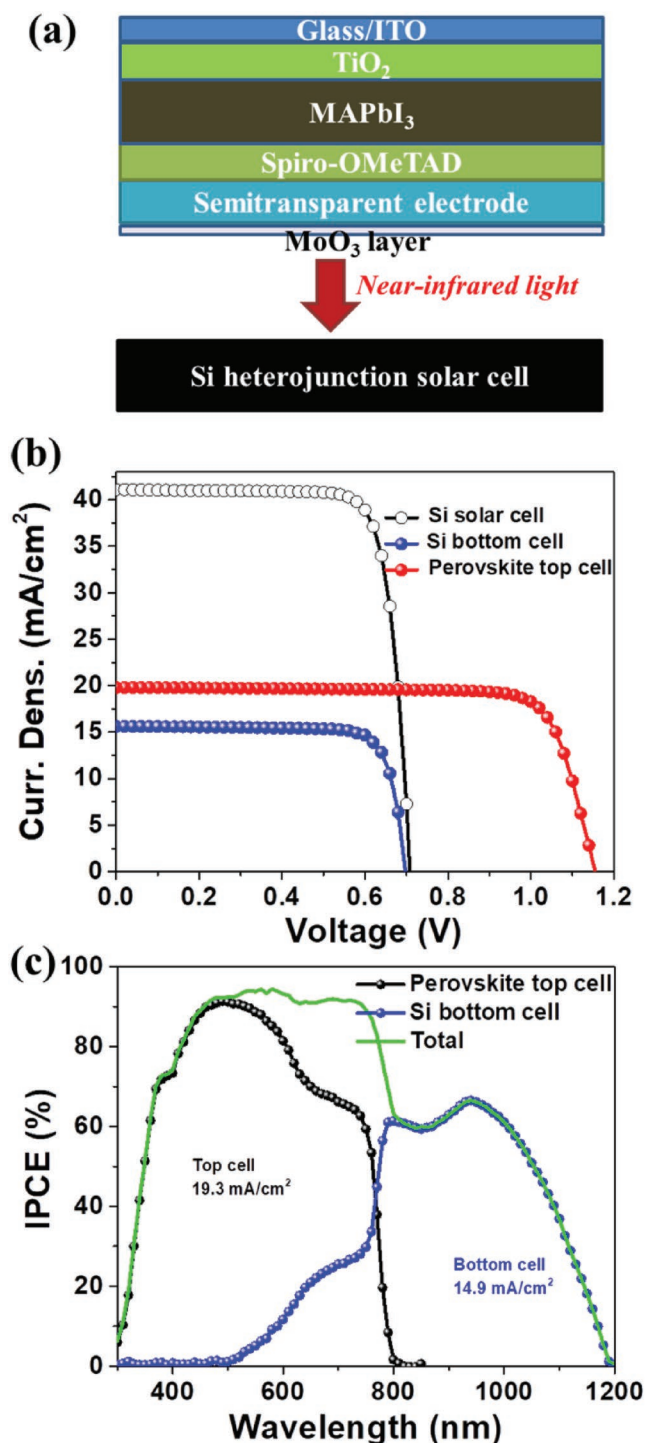


**Figure 4.** a) Schematic illustration of the 4T perovskite/silicon multijunction/tandem solar cell. b)  $J$ - $V$  curves and c) IPCE of various types of solar cells.

### 3. Conclusion

In conclusion, we demonstrate that a MoO<sub>3</sub>/Au/MoO<sub>3</sub> multilayer fabricated by thermal evaporation is an excellent transparent electrode. The good conductivity and outstanding transparency

are attributed to the gold nanomesh layer and top MoO<sub>3</sub> antireflection coating. The PCE of the semitransparent perovskite device is up to 18.3%, the highest efficiency for semitransparent Pvs-SCs to date. Combined with a heterojunction silicon solar cell, the summed efficiency of the 4T multijunction/tandem device reaches 27.0%, it is not only higher than those of component cells, but also one of the highest ever reported for this type of multijunction/tandem devices. This work adopted MAPbI<sub>3</sub> as the absorber layers to fabricate the top cell, which features a nonideal bandgap and poor stability for tandem cell-compared FA-based perovskite. These undesired properties of MAPbI<sub>3</sub> limit the efficiency and stability of tandem cell. The bandgap of FA-based perovskite absorber can be tuned by Br and Cs ions to obtain the ideal bandgap ( $\approx 1.7$  eV) for tandem cell, combined with our technology of semitransparent electrode, we believe the efficiency of tandem cell will be further improved.

### 4. Experimental Section

**Materials:** Methylamine solution (33 wt% in absolute ethanol), hydroiodic acid (HI) (57 wt% in water),  $\gamma$ -butyrolactone (GBL, 99%), and dimethyl sulfoxide (DMSO) were purchased from Aladdin. MoO<sub>3</sub> (99.5%) was purchased from Sigma Aldrich. PbI<sub>2</sub> (99.9985%) was purchased from Alfa Aesar. Spiro-OMeTAD and ITO glass were purchased from Advanced Election Technology Co., Ltd.

**CH<sub>3</sub>NH<sub>3</sub>I Synthesis:** CH<sub>3</sub>NH<sub>2</sub> and HI were mixed with the molar ratio of 1.2:1 in a round bottom flask and stirred at 0 °C for 3.5 h. The precipitate was obtained using a rotary evaporator at 60 °C to remove the solvents. The product was redissolved in absolute ethanol and precipitated by adding sufficient diethyl ether. The above step was repeated twice to obtain the purified CH<sub>3</sub>NH<sub>3</sub>I. Finally, the CH<sub>3</sub>NH<sub>3</sub>I powder was dried at 60 °C in a vacuum oven for 24 h.

**Perovskite Device Fabrication:** TiO<sub>2</sub> was deposited on ITO using a chemical bath. 4.5  $\mu$ L TiCl<sub>4</sub> was dropped onto 100 g ice surface, and then the ice was melt slowly in room temperature to form the TiCl<sub>4</sub> aqueous solution. ITO/glass was immersed into this solution, and then placed in a 80 °C hot plate for 5 min to deposit TiO<sub>2</sub> film. Finally, the samples were dried by flowing nitrogen. The perovskite absorber was deposited on TiO<sub>2</sub> using a one-step method. 645.4 mg PbI<sub>2</sub> and 222.6 mg CH<sub>3</sub>NH<sub>3</sub>I were dissolved in 1 mL of GBL and DMSO (7:3, volume/volume), with stirring at 60 °C for 6 h and filtered through a 0.45  $\mu$ m filter after cooling to room temperature. The precursor solution was spin-coated onto the TiO<sub>2</sub> substrate. The spin process consists of two consecutive steps: In the first, the spin rate was 1000 rpm for 15 s with an acceleration of 200 rpm s<sup>-1</sup>, and in the second, the spin rate was 4000 rpm for 45 s with an acceleration of 800 rpm s<sup>-1</sup>. 20 s before the end of the second step, 200  $\mu$ L chlorobenzene as antisolvent was drop-coated on the perovskite film. The film was then annealed at 100 °C for 10 min in a glove box. After cooling to room temperature, a spiro-OMeTAD solution (90 mg of spiro-OMeTAD, 36  $\mu$ L of 4-*tert*-butylpyridine, and 22  $\mu$ L of lithium bis(trifluoromethylsulfonyl)imide at 520 mg mL<sup>-1</sup> in acetonitrile dissolved in 1 mL chlorobenzene) was coated onto the perovskite film at 5000 rpm for 30 s with an acceleration of 3000 rpm s<sup>-1</sup>. The sample was kept in a desiccator overnight for the oxidation of spiro-OMeTAD. The MoO<sub>3</sub> layer was deposited onto the spiro-OMeTAD by thermal evaporation. Finally, the ultrathin Au layer was thermally evaporated onto the MoO<sub>3</sub> to be the transparent back electrode. The device area was defined by a metal mask with an aperture area of 0.096 cm<sup>2</sup>. For the top cell filter, a full area capped by a 7 nm thick Au layer was deposited onto a MoO<sub>3</sub> substrate without a mask, and a 80 nm thick MoO<sub>3</sub> film was deposited on top of the Au layer to enhance the transparency of the electrode. In this device, TiO<sub>2</sub> was approximately 30 nm, perovskite absorber was about 250 nm, and spiro-OMeTAD was

≈200 nm, those layers were measured by cross-sectional SEM. MoO<sub>3</sub>/Au/MoO<sub>3</sub> stacked layers were 30/7/80 nm, which were measured by corrected Quartz Crystal Microbalance.

**Heterojunction Silicon Solar Cells Fabrication:** Silicon devices were provided by Hanergy Company. Alkaline texturing was carried out using potassium hydroxide (KOH) to form random pyramids on both sides of an n-type silicon wafer. The sample was cleaned using the Radio Corporation of America method, and then instantly dipped into buffered oxide etch. After that, 7 nm of intrinsic amorphous silicon (a-Si:H) was deposited on the surface by plasma-enhanced chemical vapor deposition. Subsequently, both sides of the silicon wafer were treated in hydrogen plasma for a short time. Finally, 12 nm of p-type a-Si:H and 10 nm of n-type a-Si:H were deposited on the front and rear sides, respectively. On the front side, a 50 nm thick ITO layer was deposited by sputtering, and then low temperature silver paste was screen-printed onto the ITO surface through a shadow mask. The sample was annealed at 200 °C for 20 min. 15 nm of ITO was deposited by sputtering on the rear side, followed by thermal evaporation of 300 nm of MgF<sub>2</sub> as an antireflection layer and sputtering of 200 nm of silver as an electrode.

**Characterization:** The performance of the Pvs-SCs was measured using a Keithley 2400 SourceMeter under ambient conditions. The illumination intensity was calibrated to 100 mW cm<sup>-2</sup> using a National Renewable Energy Laboratory (NREL)-traceable KG5 filtered silicon reference cell. The Pvs-SCs were scanned from 1.3 to -0.1 V at a scan rate of 0.5 V s<sup>-1</sup> with a scan step of 0.02 V. The IPCE was acquired on the NREL measurement system, and the light source was a 300 W xenon lamp whose intensity was calibrated with a germanium reference photodiode. The transmission was measured using a UV-Lambda 1050 UV-vis spectrophotometer (PerkinElmer) and a UV-3600 (Shimadzu). The sheet resistance of the films was measured with the RTS-9 4-point probe resistivity measurement system (4 PROBES TECH). SEM images were obtained using a field emission SEM (FE-SEM; SU-8020, Hitachi).

## Supporting Information

Supporting Information is available from the Wiley Online Library or from the author.

## Acknowledgements

The authors acknowledge support from the National Natural Science Foundation of China (61975106/61604090), the Shaanxi Technical Innovation Guidance Project (2018HJCG-17), the National Key Research and Development Program of China (2016YFA0202403), the National University Research Fund (GK261001009), the Innovative Research Team (IRT\_14R33), the 111 Project (B14041), and the Chinese National 1000-Talents-Plan Program.

## Conflict of Interest

The authors declare no conflict of interest.

## Keywords

conductivity, multijunction/tandem, nanomesh electrodes, perovskite solar cells, transparency

Received: October 8, 2019  
Published online: November 4, 2019

[1] W. S. Yang, B.-W. Park, E. H. Jung, N. J. Jeon, Y. C. Kim, D. U. Lee, S. S. Shin, J. Seo, E. K. Kim, J. H. Noh, S. I. Seok, *Science* **2017**, 356, 1376.

- [2] D. Yang, R. Yang, K. Wang, C. Wu, X. Zhu, J. Feng, X. Ren, G. Fang, S. Priya, S. Liu, *Nat. Commun.* **2018**, 9, 3239.
- [3] X. Zhu, S. Zuo, Z. Yang, J. Feng, Z. Wang, X. Zhang, S. Priya, S. F. Liu, D. Yang, *ACS Appl. Mater. Interfaces* **2018**, 10, 39802.
- [4] NREL, Research Cell Record Efficiency Chart, <https://www.nrel.gov/pv/cell-efficiency.html> (accessed: August 2019).
- [5] J. Niu, D. Yang, X. Ren, Z. Yang, Y. Liu, X. Zhu, W. Zhao, S. Liu, *Org. Electron.* **2017**, 48, 165.
- [6] X. Zhu, Z. Xu, S. Zuo, J. Feng, Z. Wang, X. Zhang, K. Zhao, J. Zhang, H. Liu, S. Priya, S. F. Liu, D. Yang, *Energy Environ. Sci.* **2018**, 11, 3349.
- [7] D. Yang, R. Yang, S. Priya, S. Liu, *Angew. Chem., Int. Ed.* **2019**, 58, 4466.
- [8] X. Ren, D. Yang, Z. Yang, J. Feng, X. Zhu, J. Niu, Y. Liu, W. Zhao, S. F. Liu, *ACS Appl. Mater. Interfaces* **2017**, 9, 2421.
- [9] D. Yang, Z. Yang, W. Qin, Y. Zhang, S. F. Liu, C. Li, *J. Mater. Chem. A* **2015**, 3, 9401.
- [10] J. Feng, X. Zhu, Z. Yang, X. Zhang, J. Niu, Z. Wang, S. Zuo, S. Priya, S. Liu, D. Yang, *Adv. Mater.* **2018**, 30, 1801418.
- [11] D. Yang, X. Zhou, R. Yang, Z. Yang, W. Yu, X. Wang, C. Li, S. Liu, R. P. H. Chang, *Energy Environ. Sci.* **2016**, 9, 3071.
- [12] W. Shockley, H. J. Queisser, *J. Appl. Phys.* **1961**, 32, 510.
- [13] D. Zhao, C. Wang, Z. Song, Y. Yu, C. Chen, X. Zhao, K. Zhu, Y. Yan, *ACS Energy Lett.* **2018**, 3, 305.
- [14] D. H. Kim, C. P. Muzzillo, J. Tong, A. F. Palmstrom, B. W. Larson, C. Choi, S. P. Harvey, S. Glynn, J. B. Whitaker, F. Zhang, Z. Li, H. Lu, M. F. A. M. Hest, J. J. Berry, L. M. Mansfield, Y. Huang, Y. Yan, K. Zhu, *Joule* **2019**, 3, 1734.
- [15] J. Tong, Z. Song, D. H. Kim, X. Chen, C. Chen, A. F. Palmstrom, P. F. Ndione, M. O. Reese, S. P. Dunfield, O. G. Reid, J. Liu, F. Zhang, S. P. Harvey, Z. Li, S. T. Christensen, G. Teeter, D. Zhao, M. M. Al-Jassim, M. F. A. M. Hest, M. C. Beard, S. E. Shaheen, J. J. Berry, Y. Yan, K. Zhu, *Science* **2019**, 364, 475.
- [16] G. E. Eperon, M. T. Hörantner, H. J. Snaith, *Nat. Rev. Chem.* **2017**, 1, 0095.
- [17] K. A. Bush, A. F. Palmstrom, Z. S. J. Yu, M. Boccard, R. Cheacharoen, J. P. Mailoa, D. P. McMeekin, R. L. Z. Hoyer, C. D. Bailie, T. Leijtens, I. M. Peters, M. C. Minichetti, N. Rolston, R. Prasanna, S. Sofia, D. Harwood, W. Ma, F. Moghadam, H. J. Snaith, T. Buonassisi, Z. C. Holman, S. F. Bent, M. D. McGehee, *Nat. Energy* **2017**, 2, 17009.
- [18] D. Yang, R. Yang, X. Ren, X. Zhu, Z. Yang, C. Li, S. Liu, *Adv. Mater.* **2016**, 28, 5206.
- [19] D. Shi, V. Adinolfi, R. Comin, M. Yuan, E. Alarousu, A. Buin, Y. Chen, S. Hoogland, A. Rothenberger, K. Katsiev, Y. Losovyj, X. Zhang, P. A. Dowben, O. F. Mohammed, E. H. Sargent, O. M. Bakr, *Science* **2015**, 347, 519.
- [20] X. Zhu, D. Yang, R. Yang, B. Yang, Z. Yang, X. Ren, J. Zhang, J. Niu, J. Feng, S. F. Liu, *Nanoscale* **2017**, 9, 12316.
- [21] Z. Xiao, Q. Dong, C. Bi, Y. Shao, Y. Yuan, J. Huang, *Adv. Mater.* **2014**, 26, 6503.
- [22] W. H. Nguyen, C. D. Bailie, E. L. Unger, M. D. McGehee, *J. Am. Chem. Soc.* **2014**, 136, 10996.
- [23] X. Zhang, D. Yang, R. Yang, X. Zhu, J. Feng, Z. Wang, S. Zuo, J. Niu, S. Liu, *Org. Electron.* **2018**, 62, 499.
- [24] S. Ryu, J. H. Noh, N. J. Jeon, Y. C. Kim, W. S. Yang, J. Seo, S. Seok, *Energy Environ. Sci.* **2014**, 7, 2614.
- [25] D. Yang, R. Yang, J. Zhang, Z. Yang, S. Liu, C. Li, *Energy Environ. Sci.* **2015**, 8, 3208.
- [26] J. Werner, L. Barraud, A. Walter, M. Brauning, F. Sahli, D. Sacchetto, N. Tetreault, B. Paviet-Salomon, S. J. Moon, C. Allebe, M. Despeisse, S. Nicolay, S. De Wolf, B. Niesen, C. Ballif, *ACS Energy Lett.* **2016**, 1, 474.
- [27] H. Uzu, M. Ichikawa, M. Hino, K. Nakano, T. Meguro, J. L. Hernandez, H. S. Kim, N. G. Park, K. Yamamoto, *Appl. Phys. Lett.* **2015**, 106, 013506.

- [28] F. Sahli, J. Werner, B. A. Kamino, M. Bräuninger, R. Monnard, B. Paviet-Salomon, L. Barraud, L. Ding, J. J. D. Leon, D. Sacchetto, G. Cattaneo, M. Despeisse, M. Boccard, S. Nicolay, Q. Jeangros, B. Niesen, C. Ballif, *Nat. Mater.* **2018**, *17*, 820.
- [29] Oxford PV Sets World Record for Perovskite Solar Cell, <https://www.oxfordpv.com/news/oxford-pv-sets-world-record-perovskite-solar-cell> (accessed: June 2018).
- [30] Y. Yang, Q. Chen, Y.-T. Hsieh, T.-B. Song, N. De Marco, H. Zhou, *ACS Nano* **2015**, *9*, 7714.
- [31] D. Chen, H. Xi, C. Zhang, J. Chang, Z. Lin, W. Zhu, S. Pang, H. Yang, J. Zhang, L. Guo, Y. Hao, *IEEE Photonics J.* **2018**, *10*, 8400209.
- [32] C. Roldan-Carmona, O. Malinkiewicz, R. Betancur, G. Longo, C. Momblona, F. Jaramillo, L. Camacho, H. J. Bolink, *Energy Environ. Sci.* **2014**, *7*, 2968.
- [33] B. Chen, Y. Bai, Z. Yu, T. Li, X. Zheng, Q. Dong, L. Shen, M. Boccard, A. Gruverman, Z. Holman, J. Huang, *Adv. Energy Mater.* **2016**, *6*, 1601128.
- [34] G. E. Eperon, V. M. Burlakov, A. Goriely, H. J. Snaith, *ACS Nano* **2014**, *8*, 591.
- [35] Z. Ren, J. Zhou, A. Ng, Q. Shen, H. Shen, C. Surya, in *IEEE 43rd Photovoltaic Specialists Conf. IEEE, Piscataway, NJ* **2016**, 816.
- [36] M. Jaysankar, B. A. L. Raul, J. Bastos, C. Burgess, C. Weijtens, M. Creatore, T. Aernouts, Y. Kuang, R. Gehlhaar, A. Hadipour, J. Poortmans, *ACS Energy Lett.* **2019**, *4*, 259.
- [37] A. Schwier, D. Mitroo, V. F. McNeill, *Atmos. Environ.* **2012**, *54*, 490.
- [38] C. R. Amberg, *J. Am. Ceram. Soc.* **1946**, *29*, 87.
- [39] V. Nirupama, M. Chandrasekhar, P. Radhika, B. Sreedhar, S. Uthanna, *Optoelectron. Adv. Mater.* **2009**, *11*, 320.
- [40] M. Chen, R. G. Horn, *J. Colloid Interface Sci.* **2007**, *315*, 814.
- [41] F. J. Ramos, S. Jutteau, J. Posada, A. Bercegol, A. Rebai, T. Guillemot, R. Bodeux, N. Schneider, N. Loones, D. Ory, C. Broussillou, G. Goer, L. Lombez, J. Rousset, *Sci. Rep.* **2018**, *8*, 16139.
- [42] M. Liu, Z. Chen, Z. Chen, H.-L. Yip, Y. Cao, *Mater. Chem. Front.* **2019**, *3*, 496.
- [43] G. Grancini, M. K. Nazeeruddin, *Nat. Rev. Mater.* **2019**, *4*, 4.
- [44] R. A. Sinton, A. Cuevas, *Appl. Phys. Lett.* **1996**, *69*, 2510.
- [45] K. Rühle, M. K. Juhl, M. D. Abbott, M. Kasemann, *IEEE J. Photovoltaics* **2015**, *5*, 926.
- [46] D. Yang, X. Zhang, K. Wang, C. Wu, R. Yang, Y. Hou, Y. Jiang, S. Liu, S. Priya, *Nano Lett.* **2019**, *19*, 3313.